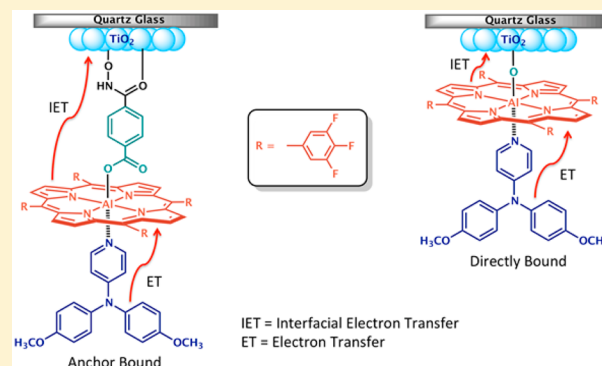


Interfacial Electron Transfer Followed by Photooxidation in *N,N*-Bis(*p*-anisole)aminopyridine–Aluminum(III) Porphyrin–Titanium(IV) Oxide Self-Assembled PhotoanodesGary N. Lim,[§] Svante Hedström,^{||} Kenneth A. Jung,^{||} Pierce A. D. Smith,[†] Victor S. Batista,^{*,||} Francis D'Souza,^{*,§} Art van der Est,^{*,‡} and Prashanth K. Poddutoori^{*,†,‡,||}[†]Department of Chemistry, University of Prince Edward Island, 550 University Ave., Charlottetown, Prince Edward Island C1A 4P3, Canada[‡]Department of Chemistry, Brock University, 1812 Sir Isaac Brock Way, St. Catharines, Ontario L2S 3A1, Canada[§]Department of Chemistry, University of North Texas, 1155 Union Circle, #305070, Denton, Texas 76203-5017, United States^{||}Department of Chemistry, Yale University, P.O. Box 208107, New Haven, Connecticut 06520-8107, United States

S Supporting Information

ABSTRACT: Two self-assembled photoanodes have been constructed by exploiting the unique optical and structural properties of aluminum(III) porphyrin (AlPor) in conjunction with TiO₂ nanoparticles as an electron acceptor and bis(*p*-anisole)-aminopyridine (BAA-Py) as an electron donor. AlPor is bound to the TiO₂ surface by either: (i) a benzohydroxamic acid bridge, in which the hydroxamic acid acts as an anchor or (ii) direct covalent binding of Al via an ether bond. The open sixth coordination site of the Al center is then used to coordinate BAA-Py through Lewis acid–base interactions, which results in donor–photosensitizer–semiconductor constructs that can be used as photoanodes. The two photoanodes were characterized by steady-state and transient spectroscopic techniques as well as computational methods. Transient-absorption studies show that in the absence of BAA-Py both the photoanodes exhibit electron injection from AlPor to the conduction band of TiO₂. However, the injection efficiencies and kinetics are strongly dependent on the linker with faster and more efficient injection occurring when the porphyrin is directly bound. Kinetic results also suggest that the recombination is faster in directly bound AlPor than benzohydroxamic acid bridged AlPor. When BAA-Py is coordinated to AlPor, electron injection from AlPor to TiO₂ is followed by electron transfer from BAA-Py to the oxidized AlPor. The injection efficiencies modeled using density functional theory and semiempirical tight-binding calculations are consistent with experimentally observed trends.



■ INTRODUCTION

Solar energy conversion is indisputably one of the most researched topics of 21st century because of the need for viable and sustainable alternatives to fossil fuels.^{1–8} One of the main approaches to this problem has been to mimic the features of natural photosynthesis in the construction of photoelectrochemical cells^{9–13} and dye-sensitized solar cells (DSSCs).^{14–18} In the light reactions of oxygenic photosynthesis, plants and cyanobacteria collect sunlight energy and convert it into chemical energy by producing adenosine triphosphate (ATP), nicotinamide adenine dinucleotide phosphate (NADPH), and molecular oxygen. This process can be imagined as a light-driven electrochemical cell in which the anodic reaction extracts electrons from water, releasing protons and oxygen, while the cathodic reaction reduces NAD⁺ and consumes protons. The resulting proton gradient within the cell is used to drive the synthesis of ATP. The objective of artificial photosynthesis

research is to construct light-driven electrochemical cells and DSSCs that can be used to produce energy-rich compounds analogous to oxygen and NADPH. Using water as the species that provides the electrons in the anodic reaction is very attractive because it is a highly abundant and nontoxic compound. However, the oxidation of water is a four-electron process and requires a potential of ~1.2 V vs NHE, which means a water oxidation catalyst (WOC) must be coupled to the photoanode. In most cases, the photoanode is fabricated by anchoring a high-potential photosensitizer on the surface of a metal oxide semiconductor.^{19–23} Upon illumination, the photosensitizer injects electrons into the conduction band of the semiconductor resulting in electron flow through the cell

Received: May 3, 2017

Revised: June 13, 2017

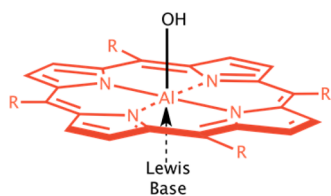
Published: June 17, 2017

and the generation of an oxidant, which removes electrons from the WOC. The latter can be codeposited with the photosensitizer on the semiconductor surface or directly linked to the photosensitizer.^{24–27} High efficiency for this process requires that the yield of electron injection by the photosensitizer should be high, while the yield of charge recombination should be low. However, this is difficult to achieve since both reactions depend on many of the same factors.

The photosensitizer in such photoanodes plays a crucial role, and ruthenium(II) polypyridyl complexes, porphyrins, or phthalocyanines have been used.^{14,19–22,24,28–33} Among the photosensitizers, porphyrins are the most versatile.³⁴ They absorb strongly in the visible region of the solar spectrum, and their chemical, physical, and redox properties can be easily tuned by inserting different central elements into the porphyrin cavity or substituting functional groups on the peripheral positions.³⁵ Furthermore, porphyrins can be anchored on metal oxide surfaces through either the peripheral or axial positions.^{22,23,31,32} Despite these attractive properties, they have not been used widely in the fabrication of photoanodes for water oxidation because most porphyrins do not generate enough oxidizing potential. However, the potential can be increased by attaching electron-withdrawing groups to the periphery of the porphyrin^{21,23,26,27} or inserting an electro-positive element into the porphyrin ring.²⁵ Recently, we reported high-potential photoanodes based on phosphorus(V) porphyrin (PPor) and tin(IV) oxide (SnO₂) semiconductor²⁵ and showed that PPor was able to photooxidize a water oxidation precatalyst which was codeposited on the SnO₂ surface. The efficiency of electron injection into the semiconductor and the solar cell efficiency were found to depend strongly on how the porphyrin was anchored to the surface. Thus, a more thorough investigation of different modes of coupling the photosensitizer to the metal oxide and secondary donor is needed.

Here, we explore the use of aluminum(III) porphyrin (AlPor) as a photosensitizer in high-potential photoanodes. Among the porphyrins, AlPor is unique (see Chart 1) because

Chart 1. Bonding Modes of Aluminum(III) Porphyrin



the Al center can form an axial covalent bond on one face of the porphyrin ring and a coordination bond on opposite face.^{35–42} These two axial-bonding modes are ideally suited for attaching the AlPor to a metal oxide surface and coordinating a secondary donor or water oxidation catalyst. Compared to PPor, AlPor is not as oxidizing, but with electron-withdrawing substituents it can be made sufficiently electropositive to be used in high-potential photoanodes for water oxidation. We have constructed two supramolecular self-assembled photoanodes in which AlPor is covalently bound to a titanium(IV) oxide (TiO₂) surface via either a direct ether linkage or a benzohydroxamic acid bridge. Hydroxamate was chosen as the anchor due to its efficient anchoring and photoconversion properties.^{43,44} The other side of the AlPor is coordinated with the secondary electron donor bis(*p*-aniso)aminopyridine

(BAA–Py) via Lewis acid–based interaction. The newly fabricated photoanodes have been characterized by steady-state spectroscopic techniques, and their optical properties have been investigated using transient spectroscopic methods. These self-assembled photoanodes allow the investigation of sequential electron injection along a direction perpendicular to the porphyrin plane. The optical properties of BAA⁺, AlPor⁺, and Ti(III) make it possible to easily detect the formation of BAA⁺–AlPor–Ti(III)O₂ by transient absorption spectroscopy allowing the kinetics and efficiency of the electron injection and hole transfer processes to be estimated. We have also used density functional theory (DFT) calculations to elucidate the electronic properties that are important for effective injection of photoexcited electrons from the adsorbate to the semiconductor.

EXPERIMENTAL SECTION

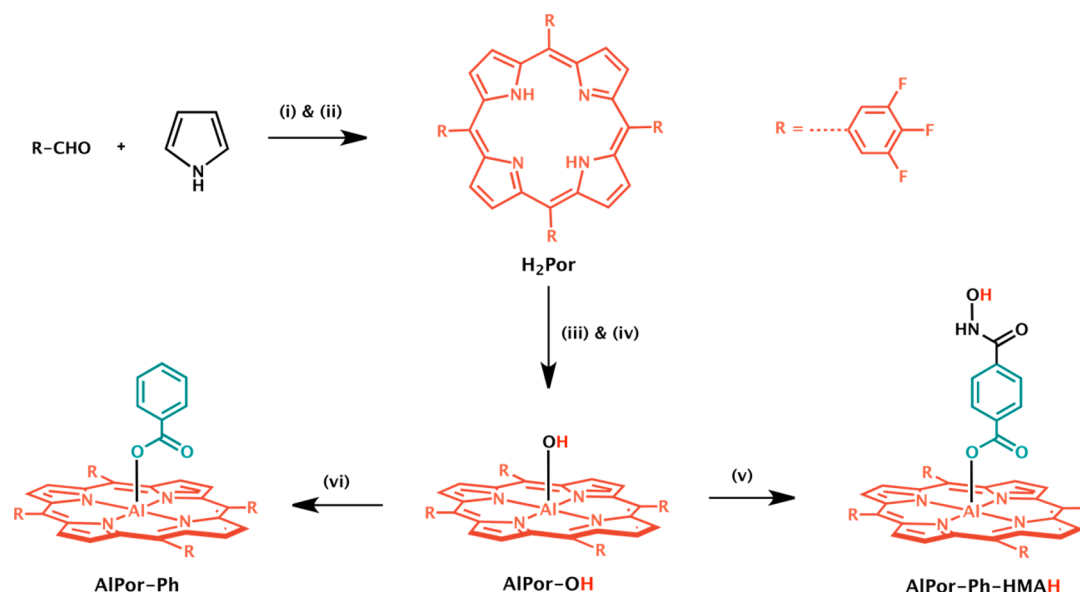
Synthesis. All of the chemicals, solvents, and chromatographic materials were obtained from Sigma-Aldrich Chemicals and were used as received. The TiO₂ (Aeroxide P25) was obtained from Evonik Industries. The supporting electrolyte, tetra-*n*-butylammoniumperchlorate (TBAP), for electrochemistry studies was purchased from Fluka Chemicals. The synthesis of the precursor porphyrins 5,10,15,20-tetrakis-(3,4,5-trifluorophenyl)porphyrin (H₂Por), and its Al(III) derivative 5,10,15,20-tetrakis(3,4,5-trifluorophenyl)-porphyrinatoaluminum(III) hydroxide (AlPor–OH), was carried out according to the literature procedures.^{40,41,45} The investigated porphyrin derivatives and the secondary electron donor bis(*p*-aniso)aminopyridine (BAA–Py) were synthesized according to Schemes 1 and 2; for details see the Supporting Information.

METHODS

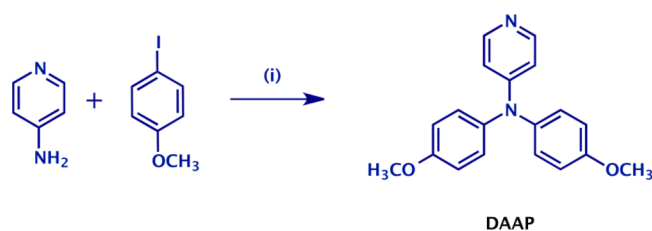
NMR and Mass Spectroscopy. NMR spectra were recorded with Bruker Avance 300 and 600 MHz digital NMR spectrometers using CDCl₃, DMSO-*d*₆, and/or CD₃OD as the solvent. FAB mass spectra were recorded on a Kratos Concept 1S high-resolution E/B mass spectrometer.

Electrochemistry. Cyclic and differential pulse voltammetric experiments [CH₂Cl₂, 0.1 M tetrabutylammonium perchlorate, (TBAP)] were performed on a BAS Epsilon electrochemical analyzer (working electrode: glassy carbon, auxiliary electrodes: Pt wire, reference electrode: Ag wire). The Fc⁺/Fc (Fc = ferrocene) couple was used to calibrate the redox potential values, $E_{1/2}(\text{Fc}^+/\text{Fc}) = 0.48 \text{ V vs SCE in CH}_2\text{Cl}_2$, 0.1 M TBAP under our experimental conditions. The redox potentials were reported vs NHE (= SCE + 0.24 V). Spectroelectrochemical studies were performed by using a cell assembly (SEC-C) supplied by ALS Co., Ltd. (Tokyo, Japan). This assembly is comprised of a Pt counter electrode, a 6 mm × 6 mm Pt gauze working electrode, and an Ag/AgCl reference electrode in a 1.0 mm path length quartz cell. The optical transmission was limited to 6 mm × 6 mm covering the Pt gauze working electrode.

Absorption Spectroscopy. Solution state UV–vis absorption spectra were recorded with a ThermoSpectronic/Unicam UV-4 UV–vis spectrometer. Concentration of the samples used for these measurements ranged from 10^{–6} M (for measuring the porphyrin Soret band) to 10^{–5} M (for measuring the porphyrin Q-bands) solutions. Surface bound solid-state UV–

Scheme 1. Synthesis of Investigated Compounds^a

^aReaction conditions: (i) $\text{BF}_3 \cdot \text{OEt}_2$, stir in dry CH_2Cl_2 for 2 h at 35 °C under N_2 , (ii) *p*-chloranil, stir for 3 h at room temperature, (iii) AlMe_3 , stir in dry toluene for 5 days at room temperature under N_2 , (iv) water, stir for 12 h at room temperature, (v) HOOC-Ph-HMAH , stir in CH_2Cl_2 (with a few drops of CH_3OH) for 12 h at room temperature under N_2 , (vi) Ph-COOH , stir in CH_2Cl_2 for 12 h at room temperature under N_2 .

Scheme 2. Synthesis of BAA-Py^a

^aReaction conditions: (i) 1,10-phenantroline, CuI , KOH , toluene, reflux for 48 h under nitrogen.

vis absorption spectra were recorded on a Jasco V-670 spectrophotometer.

Preparation of Thin Films of Dye-Sensitized TiO_2 . TiO_2 nanoparticles (Aeroxide P25) were mixed into a paste by combining 1.0 g of dry nanoparticles with 2 mL of H_2O and 2 mL of EtOH . The paste was then doctor-bladed onto 1 mm thick fused silica microscope slides (1×1 in, GM Associates). The resulting films were then sintered in air at 450 °C for 2 h. The anchor-bound photoanodes (AlPor-Ph-TiO_2) were prepared by soaking the bare semiconductor films for 12 h in a 0.1 mM solution of AlPor-Ph-HMAH in CH_2Cl_2 containing few drops of methanol. The directly bound photoanodes (AlPor-TiO_2) were prepared by soaking the films in a 0.1 mM solution of AlPor-OH in benzene at 80 °C for 12 h. The same sensitized films were also used to collect absorption spectra of the dye on the semiconductor surface.

Fluorescence Spectroscopy. Steady-state fluorescence spectra were recorded using a Photon Technologies International (London, Ontario) Quanta Master model QM-2001 L-format, equipped with double-grating monochromators, a 150 W xenon lamp, running Felix 32 software. An excitation wavelength of 550 nm, which selectively excites the porphyrin, was used, and the concentrations were held constant for all the compounds. The lifetimes were measured with the time

correlated single photon counting (TCSPC) lifetime option with nano-LED excitation sources on a Horiba Jobin Yvon Nanolog. A right angle detection method was used.

Absorption and Fluorescence Titrations. Absorption titrations were carried out in CH_2Cl_2 at concentrations appropriate for measuring the porphyrin Soret band. A solution containing AlPor-Ph was placed in a cuvette and titrated by adding aliquots of a concentrated solution of the BAA-Py. The BAA-Py solution also contained AlPor-Ph at its initial concentration so that the porphyrin concentration remained constant throughout the titration. The binding constants were calculated by fitting the equation⁴⁶

$$\Delta A_{600} = \frac{\varepsilon}{2} \left[\left([\text{AlPor}] + [\text{D}] + \frac{1}{K} \right) - \sqrt{\left([\text{AlPor}] + [\text{D}] + \frac{1}{K} \right)^2 - 4[\text{AlPor}][\text{D}]} \right] \quad (1)$$

to ΔA_{600} , the measured change in the absorbance at 600 nm. $[\text{AlPor}]$ is the total concentration of AlPor-Ph ; $[\text{D}]$ is the total concentration of the donor either BAA-Py or Py, which is varied; K is a binding constant, and ε is the molar absorptivity of the D- AlPor-Ph complex. In an analogous manner, steady-state fluorescence titrations were carried out in CH_2Cl_2 using solutions at a constant concentration of AlPor-Ph and varying concentrations of BAA-Py. The solutions were excited at the isosbestic point wavelength, which was obtained from the corresponding absorption titrations.

Femtosecond Transient Absorption Spectroscopy. Femtosecond transient absorption spectroscopy experiments were performed using an ultrafast femtosecond laser source (Libra) by Coherent incorporating a diode-pumped, mode-locked Ti:sapphire laser (Vitesse) and diode-pumped intracavity doubled Nd:YLF laser (Evolution) to generate a compressed laser output of 1.45 W. For optical detection, a

Helios transient absorption spectrometer coupled with a femtosecond harmonics generator, both provided by Ultrafast Systems LLC, was used. The source for the pump and probe pulses was derived from the fundamental output of Libra (compressed output 1.45 W, pulse width 90 fs) at a repetition rate of 1 kHz. 95% of the fundamental output of the laser was introduced into a harmonic generator which produced second and third harmonics of 400 and 267 nm besides the fundamental 800 nm for excitation, while the rest of the output was used for generation of the white light continuum. In the present study, the second harmonic 400 nm excitation pump was used in all of the experiments. Kinetic traces at appropriate wavelengths were assembled from the time-resolved spectral data. Data analysis was performed using Surface Explorer software supplied by Ultrafast Systems.

Computational Methods. AlPor–OH and AlPor–Ph–HMAH were subjected to density functional theory (DFT) quantum chemistry calculations using the Gaussian09 software,⁴⁷ in the presence of a CH₂Cl₂ polarizable continuum implicit solvent model.⁴⁸ Optimizations and subsequent frequency calculations were performed on the ground state, the oxidized state, and the reduced state of the two molecules using the B3LYP functional⁴⁹ and 6-31G(d,p) basis set, followed by single point calculations with the 6-311+G(2d,p) basis set. Calculated redox potentials were obtained by first estimating the free energy of each species by adding the free energies of vibration, rotation, and translation to the electronic energy, then taking the free energy difference between the neutral and respectively oxidized or reduced form. This was referenced to NHE by assuming a 4.44 V absolute potential of NHE,⁵⁰ and using the known redox potentials of a free-base porphyrin⁵¹ as an additional reference. AlPor–OH and AlPor–Ph–HMAH underwent linear-response time-dependent (TD)-DFT calculations at the B3LYP/6-31+G(d,p)//6-31G(d,p) level of theory in CH₂Cl₂ to investigate their UV–visible absorption down to 300 nm. No vibronic effects were taken into account. The CAM-B3LYP functional⁵² was also tested for calculating redox properties and UV–visible absorption, yielding poorer agreement with experiments. The first triplet state T₁ of AlPor–OH was investigated at the B3LYP/6-311+G(2d,p)//6-31G(d,p) level of theory in *ortho*-dichlorobenzene (*o*-DCB) solvent, followed by a single point calculation of the ground state S₀ at the T₁ geometry, at the same level of theory.

Electron Injection Calculations. The injection of photo-excited electrons into anatase TiO₂ was studied computationally on semioptimized porphyrin–TiO₂ model systems, using a previously reported electron-propagation scheme based on extended Hückel theory.⁵³ The model systems were created by first replacing the trifluorophenyl groups on AlPor–OH with hydrogen atoms and then attaching it in a monodentate fashion via its deprotonated hydroxyl group directly to the 101 surface of an anatase Ti₂₀O₄₀ cluster. The Ph–HMA linker was bidentate-bound via its deprotonated hydroxamic acid anchoring group to an identical Ti₂₀O₄₀ cluster. These two systems, AlPor–Ti₂₀O₄₀ and Ph–Ti₂₀O₄₀, were then optimized at the B3LYP/LANL2DZ level of theory, allowing the adsorbate and the TiO₂ atoms within 2 bonds of the adsorbates to relax while the remaining TiO₂ atoms were kept frozen in the crystal geometry. The truncated systems: AlPor–Ti₂₀O₄₀ and Ph–Ti₂₀O₄₀ are sufficient to obtain good binding geometries, but for the injection calculations, the full molecular adsorbate structures are necessary. Hence, we reattach the meso-

substituents in the AlPor–Ti₂₀O₄₀ case and the full porphyrin ring in the Ph–Ti₂₀O₄₀ case according to their geometries as fully optimized for the molecular systems without the semiconductor. Finally, the anatase was extended according to its crystal structure to a periodic slab of Ti₁₂₈O₂₅₆, as shown in Figure 1. On the two respective systems, a wave packet was

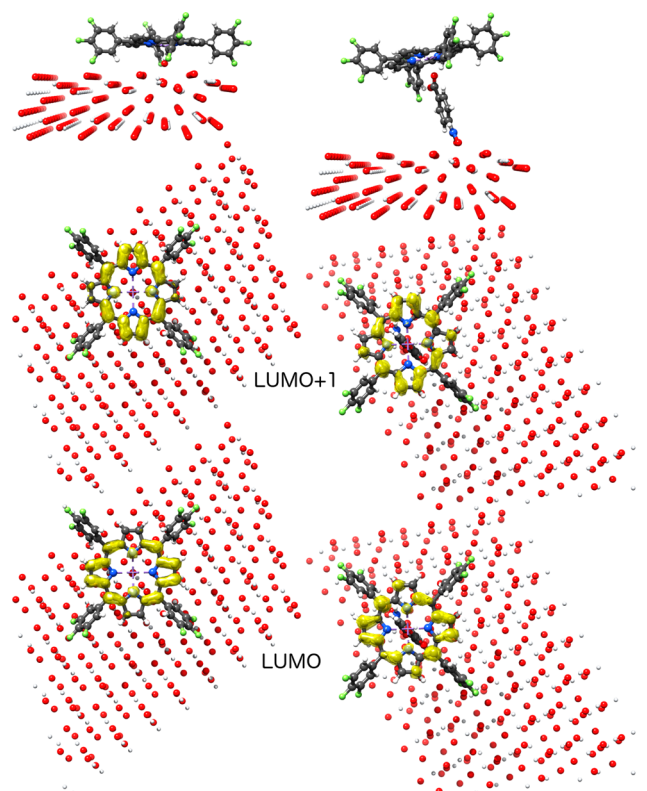


Figure 1. Semioptimized AlPor–Ti₂₀O₄₀ (left) and AlPor–Ph–Ti₁₂₈O₂₅₆ (right) systems used for injection calculations, shown from the side and from the top with the initial density of the extended Hückel wave packets, corresponding to the square of the LUMO+1 or LUMO, exhibiting perfect agreement with the corresponding orbitals from DFT shown in Figure S5.

initialized on the adsorbate LUMO and LUMO+1 respectively, which are the orbitals populated at the pump wavelength in the TA experiments. These orbitals were verified by comparing their character to those obtained from more rigorous DFT calculations. The wave packet is then allowed to propagate through the system according to the equation:

$$|\Psi(t)\rangle = \sum_k \langle \phi_k | \Psi(0) \rangle e^{-iE_k t / \hbar} |\phi_k\rangle \quad (2)$$

where ϕ_k are the orbitals with eigenenergies E_k as obtained from the YaEHMOP extended Hückel software.⁵⁴ The wave packet $\Psi(t)$ at time t is obtained by integrating this equation in time steps of 1.0 fs for 3500 fs. To compensate for the finite dimensions of our TiO₂ model, absorbing potentials were added to the Ti atoms on the bottom and side edges of the cluster to simulate the electron density dissipating in the nanoparticle. While extended Hückel typically describes the electronic structure within a single material adequately, the empirical parameters are referenced to different vacuum states depending on the material. Therefore, we shifted the adsorbate orbitals up in energy compared to the TiO₂ states, to confer the

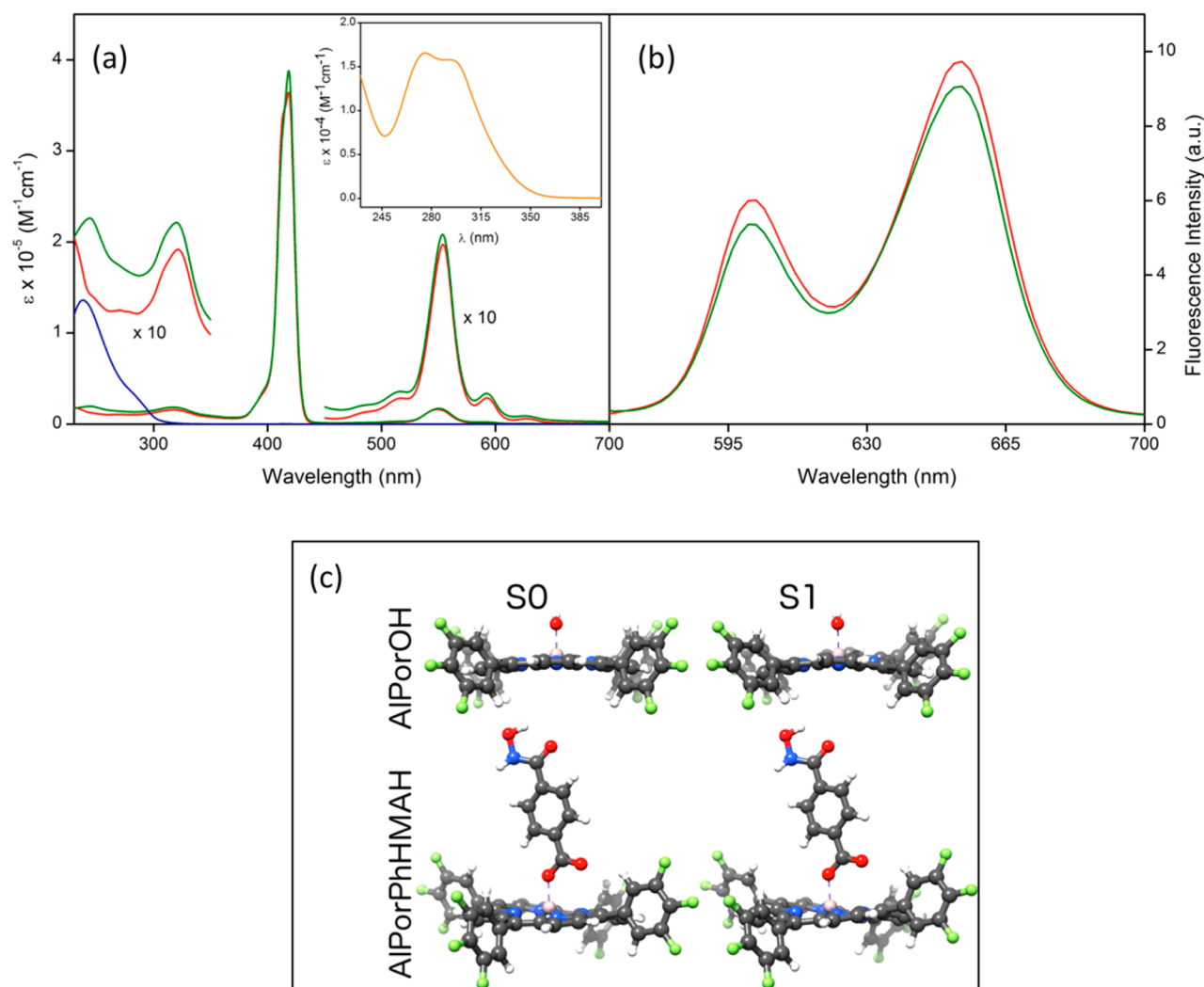


Figure 2. Optical spectra of AlPor-Ph-HMAH (green) and its reference compounds AlPor-Ph (red) and HOOC-Ph-HMAH (blue). (a) Absorption spectra, the inset shows the absorption spectrum of BAA-Py (orange). (b) Fluorescence spectra measured with an excitation wavelength of 550 nm. All spectra were measured in CH₂Cl₂. For solubility reasons a small amount of CH₃OH was added to the solutions of AlPor-Ph-HMAH, AlPor-Ph, and HOOC-Ph-HMAH. (c) Side views of the optimized geometries of the ground S₀ state and the excited S₁ state of AlPor-OH and AlPor-Ph-HMAH, demonstrating that in both cases S₁ is less planar than S₀, which accounts for the redshift of the emission compared to absorption.

same driving force for injection as obtained from DFT calculations.

RESULTS AND DISCUSSION

Synthesis. As shown in Scheme 1, 5,10,15,20-tetrakis(3,4,5-trifluorophenyl)porphyrinatoaluminum(III) hydroxide (AlPor-OH) was prepared by the condensation of 3,4,5-trifluorobenzaldehyde and pyrrole followed by the insertion of the Al center. The electron-withdrawing fluorine atoms on the meso-phenyl groups increase the oxidation potential of the porphyrin. This also lowers the energy of the excited singlet state making it well-poised for injection of electrons into the conduction band of TiO₂ as well as the photooxidation of BAA-Py. The new compounds AlPor-Ph-HMAH and AlPor-Ph were prepared in quantitative yields by the condensation of AlPor-OH with HMAH-Ph-COOH and Ph-COOH, respectively; for details, see Supporting Information. Benzylhydroxamic acid was chosen for the anchor because dye-sensitized solar cells constructed using hydroxamates to bind the dye to TiO₂ show better performance than those made

using carboxylates or phosphates.⁴³ With AlPor bound to TiO₂, Lewis acid–base interactions between pyridine of BAA-Py and Al center of AlPor were then exploited to construct the BAA-Py–AlPor–Ph–TiO₂ and BAA-Py–AlPor–TiO₂ photoanodes. The structural characterization of the porphyrins was performed with various spectroscopic techniques as described in the Supporting Information.

UV–Visible Absorption and Fluorescence Spectroscopy. The UV–visible spectra of AlPor-Ph-HMAH and its reference compounds AlPor-Ph and HMAH-Ph-COOH (Figure 2) were measured in CH₂Cl₂ with a small amount of methanol, which is needed for solubility reasons. As is typical for porphyrins, the absorption spectra (Figure 2a) show a strong B-band (or Soret band) at ~420 nm and a weaker Q-band at ~550 nm. The Q-band is split into several vibronic components. According to our TD-DFT calculations both bands corresponds to linear combinations of the HOMO → LUMO, HOMO → LUMO+1, HOMO–1 → LUMO, and HOMO–1 → LUMO+1 transitions. For the Q-band, the major contribution is from the transitions originating from the

Table 1. Optical and Redox Data of the Investigated Compounds in CH_2Cl_2 ^a

sample	potential [V vs NHE]		absorption λ_{max} (nm) { $\log[\epsilon \text{ (M}^{-1} \text{ cm}^{-1})]$ }				fluorescence	
	oxidation	reduction	B-band	Q-band	axial ligand		λ_{max} nm	
AlPor–Ph–HMAH	exp. 1.31, 1.62	–0.80, –1.23	418 (5.59)	593 (3.53), 554 (4.32), 514 (3.55)	319 (4.34), 243 (4.35)		602, 654	
	calc. 1.48	–0.63	399 (5.64)	542 (2.81)	298 (4.70)		565	
AlPor–Ph	exp. 1.28, 1.54	–0.79, –1.19	418 (5.56)	593 (3.46), 554 (4.30), 514 (3.44)	321 (4.28)		602, 654	
	calc. ^b 1.45	–0.66	401 (5.67)	544 (3.13)	301 (4.80)		571	
HMAH–Ph–COOH					280 (3.56), 238 (4.13)			
BAA–Py	1.24				295 (4.20), 275 (4.22)		474	

^aFor solubility reasons a small amount of methanol was added to absorption and fluorescence solutions. ^bAlPor–OH.

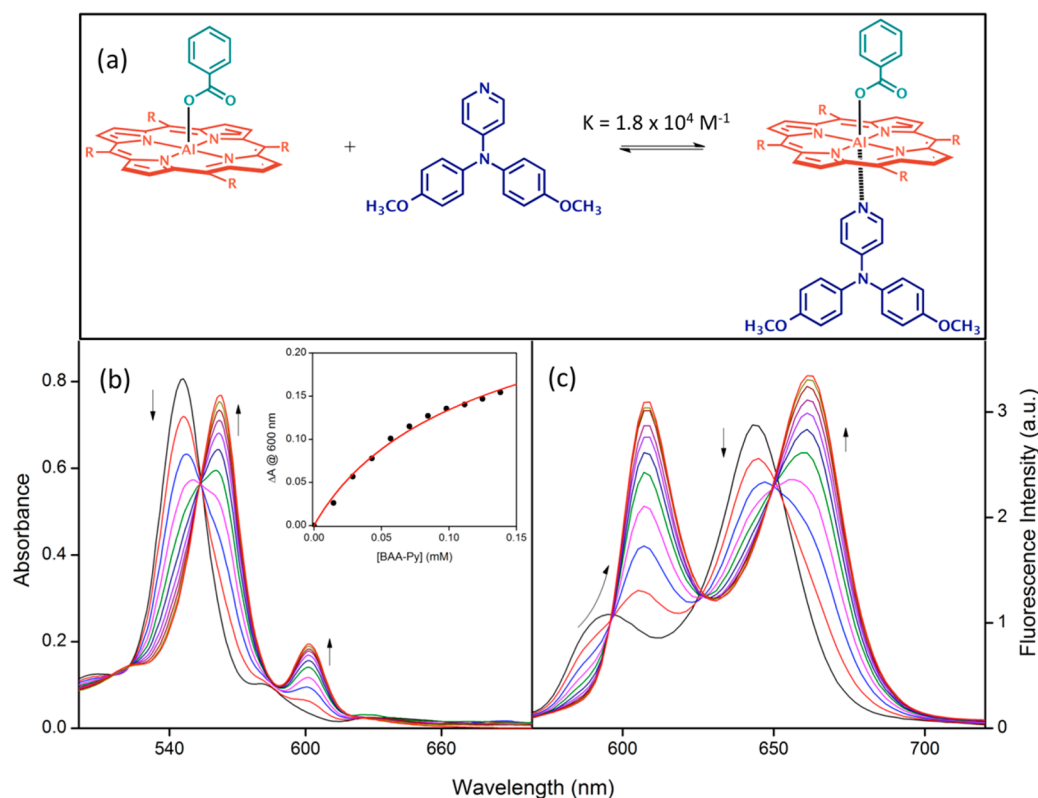


Figure 3. (a) Represents the formation of dyad BAA–Py–AlPor–Ph in CH_2Cl_2 . (b) Absorption and (c) fluorescence titrations of AlPor–Ph with BAA–Py in CH_2Cl_2 . The inset shows a plot of the change of absorbance at 600 nm and the fit for formation of a 1:1 complex (eq 1). BAA–Py was added up to 1.38×10^{-4} M in $5 \mu\text{L}$ (1.44×10^{-5} M) increments to 1 mL (6×10^{-5} M) solution of AlPor–Ph. The excitation wavelength was chosen at the isosbestic point, 555 nm, which was obtained from absorption titrations.

HOMO, while for the B-band the transitions from the HOMO–1 are dominant. The band positions and their molar extinction coefficients are summarized in Table 1, and the composition of the bands obtained from the DFT calculations are given in Table S1. Isodensity plots of the frontier orbitals are shown in Figure S5. The calculated frequencies and transition probabilities are in good agreement with experiments, except the intensity of the Q-band, which is underestimated because the TD-DFT calculations were performed without vibronic considerations. The fluorescence wavelength is underestimated in calculations for the same reason. The calculations suggest that the Stokes shift of the porphyrin fluorescence is largely the result of a loss of planarity of the porphyrin ring in the S_1 state as illustrated by the calculated structures shown in Figure 2c. As shown in Figure 2a and Table 1, the absorption spectrum of the dyad is essentially a linear combination of its reference compounds. Furthermore, the band positions and molar extinction coefficients (ϵ) and

fluorescence intensities of the dyad are similar to those of the corresponding monomer porphyrin. Thus, we can conclude that the electronic structures of the basal porphyrin (AlPor) and axial unit (HMAH) are not perturbed strongly when they are attached to one another. This is expected because their perpendicular relative orientation does not allow significant orbital overlap between the respective π -systems. The Py-appended donor, BAA–Py, has relatively weak and very broad absorption bands in ultraviolet region (Figure 2a inset). Thus, the absorption band of AlPor at 550 nm, which is well apart from the BAA–Py bands, can be used to selectively excite the AlPor. A comparison of the fluorescence spectra, Figure 2b, of AlPor–Ph and AlPor–Ph–HMAH reveals that the axial HMAH unit has no significant influence on the decay processes in AlPor.

Figure 3 shows absorption and fluorescence titrations of the coordination of BAA–Py to AlPor–Ph to form the dyad BAA–Py–AlPor–Ph. Upon addition of BAA–Py, the Q bands of the

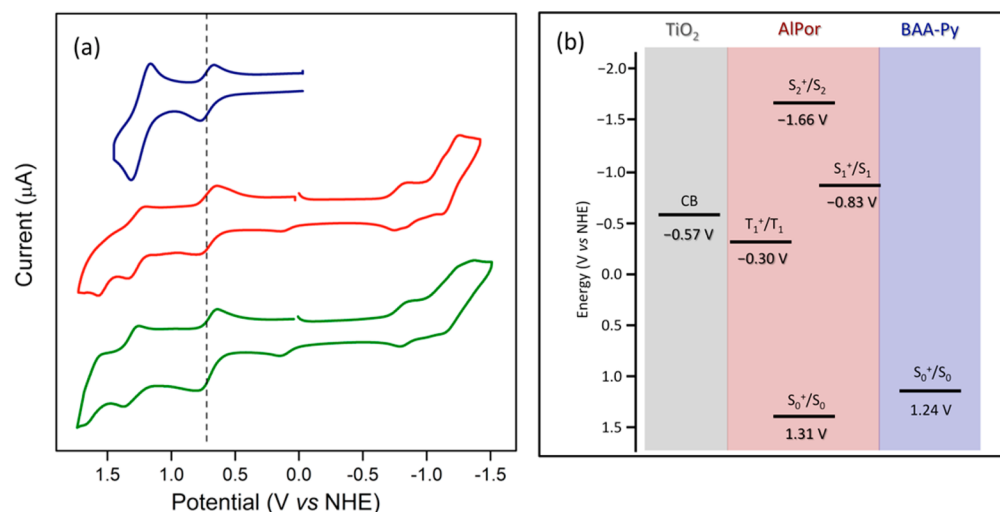


Figure 4. (a) Cyclic voltammograms of AlPor-Ph (red), AlPor-Ph-HMAH (green), and BAA-Py (blue) with 0.1 M TBA.ClO₄ in CH₂Cl₂. Data were measured with ferrocene (0.72 V vs NHE) as an internal standard. The scan rate was 200 mV/s. (b) Energy level diagram of the photo- and redox-active units (AlPor, BAA-Py, TiO₂, and SnO₂). Here CB, S, and T represent the conduction band, singlet state, and triplet state energies, respectively.

porphyrin 554 and 593 nm are shifted to 561 and 600 nm (Figure 3b), and a corresponding shift of the fluorescence bands is also observed (Figure 3c) both of which are typical of axial coordination of nitrogen ligands to AlPors.^{35,38–42} For comparison, the corresponding titrations with pyridine are shown in Figure S7. In both cases an isosbestic point is observed in the absorption titration at 555 nm, and the absorbance change is fit well assuming that a 1:1 complex is formed (insets in Figure 3b and S7a). The binding constant, $K = 1.8 \times 10^4 \text{ M}^{-1}$, obtained from the fit in Figure 3b is about one order magnitude higher than for coordination of Py ligands to other AlPors^{37,38,41,42} because the electron-withdrawing 3,4,5-trifluorophenyl substituents on the porphyrin make the Al center a much better Lewis acid. Figure S6 shows the ¹H NMR spectrum of a 1:1 mixture of AlPor-Ph and BAA-Py (bottom) along with the individual spectra of AlPor-Ph (middle) and BAA-Py (top). In the dyad complex, BAA-Py-AlPor-Ph, shielding due to the porphyrin ring causes an upfield shift of the BAA-Py protons on the pyridine unit and *p*-cresol moiety. The magnitude of the shift depends on the distance of the protons from the porphyrin ring; hence the pyridinyl protons display the large shift indicating that coordination occurs via the pyridinyl group. On the axial benzoate group of the AlPor, the protons closest to the porphyrin ring show an increased upfield shift upon coordination, suggesting that the aluminum(III) center lies out of the porphyrin plane in AlPor-Ph and is pulled into the plane when BAA-Py coordinates. Together, the absorption and fluorescence titrations and NMR data firmly establish formation of the dyad BAA-Py-AlPor-Ph in solution. However, the fact that the binding does not lead to quenching of the fluorescence (Figures 3c and S7b) indicates that electron transfer from BAA to the excited state of AlPor does not occur to any significant extent despite the fact that this step is predicted to be exergonic (see below).

Electrochemistry. Cyclic voltammograms of the newly synthesized compounds were measured with 0.1 M TBA.ClO₄ in CH₂Cl₂. Ferrocene was an internal standard (Figure 4a, Table 1). The redox changes of all of the compounds are found to be one-electron reversible processes based on the peak-to-peak separation values and the cathodic-to-anodic peak current

ratio. During the cathodic scans of AlPor-Ph-HMAH and AlPor-Ph, the first and second reductions of the AlPor unit are observed, while the anodic scan shows the first and second oxidation of AlPor. The corresponding DFT-calculated redox potentials are in fair agreement with experiments, as seen in Table 1. Figure S5 shows the calculated spin density of the reduced and oxidized states, showing that the first reduction/oxidation respectively adds/removes an electron to/from the LUMO/HOMO–1. As anticipated, the measured and calculated redox potentials do not depend significantly on the nature of the axial ligand because of the poor overlap of the linker and porphyrin π -orbitals. BAA-Py shows a one-electron reversible process which corresponding to its first oxidation and is about 70 mV lower than that of AlPor.

Energy Level Diagram. The redox potentials are used in combination with optical data to construct the energy level diagram of the states involved in possible electron-transfer processes. Figure 4b summarizes the energy levels of the investigated compounds. For AlPor, the potential for oxidation of the ground state is 1.31 V vs NHE. The blue edge of the fluorescence spectra (see Figure 2b) at 594 nm places the lowest excited singlet state 2.14 eV above the ground state at a potential of –0.83 V vs NHE. The blue edge of the phosphorescence spectrum of the AlPor yields an energy of 1.61 eV above the ground state for the lowest excited triplet state, which places it at –0.30 V vs NHE. In the absorption spectrum, the Soret band at 418 nm (2.97 eV) corresponds to the energy gap between the ground state and the second excited singlet state of AlPor. Using the singlet and triplet energies as well as conduction band edge energy of the TiO₂ (–0.57 V vs NHE)⁵⁵ the energy level diagram as shown in Figure 4b was constructed. From this diagram, it is evident that the porphyrin is well-positioned to inject electrons into the conduction band as well as to photooxidize the coordinated BAA-Py unit.

AlPor Surface Binding Studies. As described in the Experimental Section photoanodes were prepared by attaching AlPor to a thin film of TiO₂ nanoparticles on a fused silica microscope slide. AlPor-Ph-HMAH was bound to the surface by the formation of coordination bonds between Ti and O

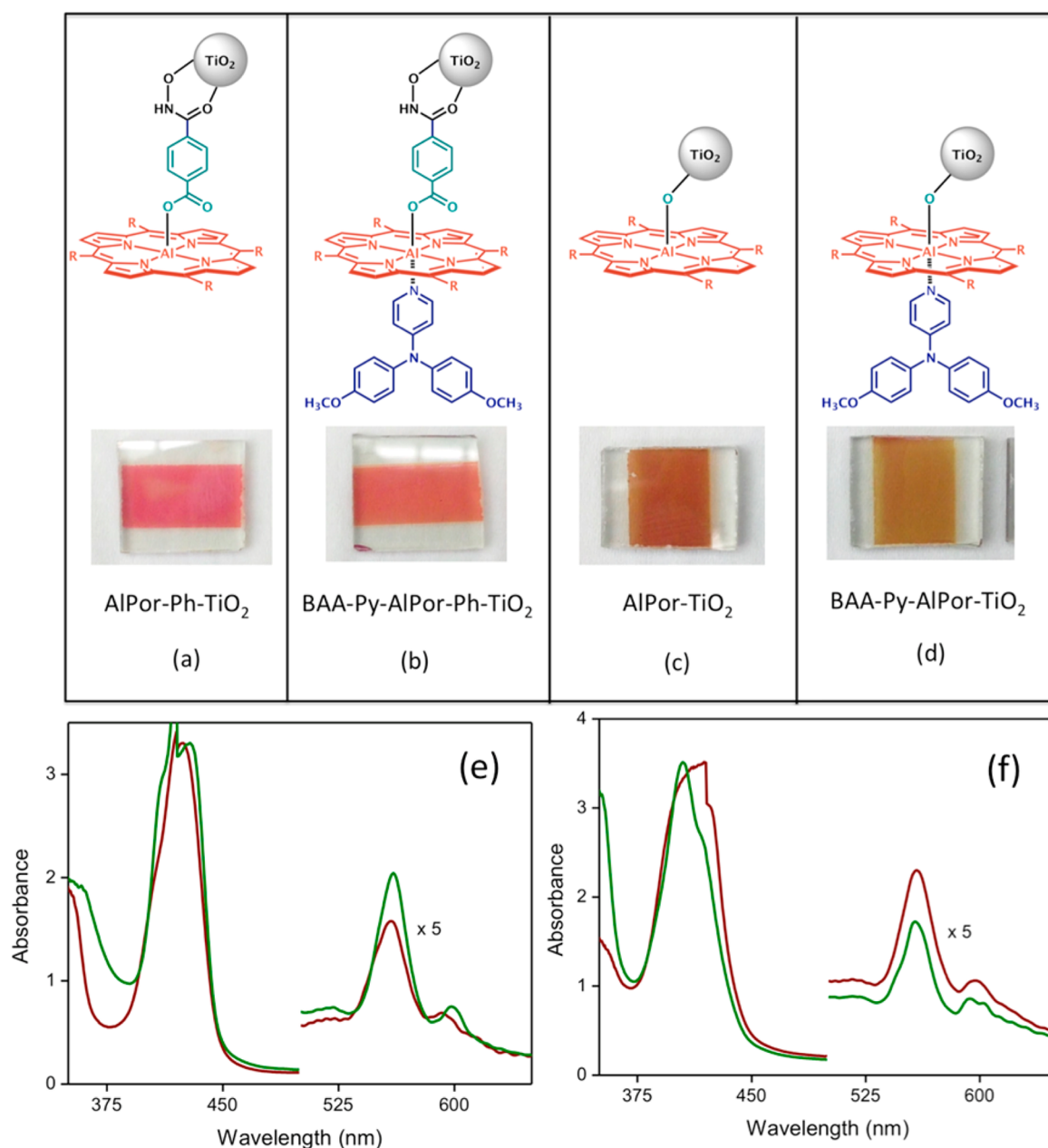


Figure 5. Top a–d: Anchoring modes and investigated photoanodes. Bottom: (e) absorption spectra of AlPor–Ph–TiO₂ (maroon) and BAA–Py–AlPor–Ph–TiO₂ (green) and (f) absorption spectra of AlPor–TiO₂ (maroon) and BAA–Py–AlPor–TiO₂ (green).

atoms of the hydroxamate group (HMA) (Figure 5a). In contrast, with AlPor–OH, displacement of the axial OH group by active OH groups on the surface (Ti–OH) results in a covalent Al–O–Ti bond, which directly binds the porphyrin to the surface without any spacer (Figure 5c). The hydroxamate binding is achieved by soaking the bare semiconductor film in a solution of the porphyrin at room temperature for 12 h. However, in the case of AlPor–OH, the temperature must be raised to 80 °C for binding to occur. After attachment of the porphyrin to the electrode surface, BAA–Py was coordinated by soaking the anodes in BAA–Py solutions (Figure 5b and d). The UV–visible absorption spectra of the resulting constructs are shown in Figure 5e and f. The positions of the porphyrin bands are the same as observed in solution (see Figure 2), but broadening of the Soret band is observed. This suggests that

the electronic structure of AlPor is perturbed by the binding as well as the solid-state nature of the sample.

Spectroelectrochemistry. Before studying the performance of the electrodes, spectroelectrochemical studies were carried out on AlPor–Ph and BAA–Py in *o*-DCB containing 0.2 M TBA·ClO₄ to help interpret the transient spectral data of the products formed during the process of charge injection. As shown in Figure 6a, during the first oxidation of AlPor–Ph, the B-band and Q-bands of the neutral porphyrin at 418 and 554 nm lose intensity, and new peaks due to the AlPor–Ph radical cation appear at 595 and 690 nm. Isosbestic points at 415, 540, and 571 nm were also observed. During the first reduction of AlPor–Ph, the peaks of the neutral porphyrin decrease, and new peaks due to the radical anion appear at 433, 568, and 608 nm. Isosbestic points at 428 and 562 nm were also observed (Figure 6b). As shown in Figure 6c, the weak radical cation

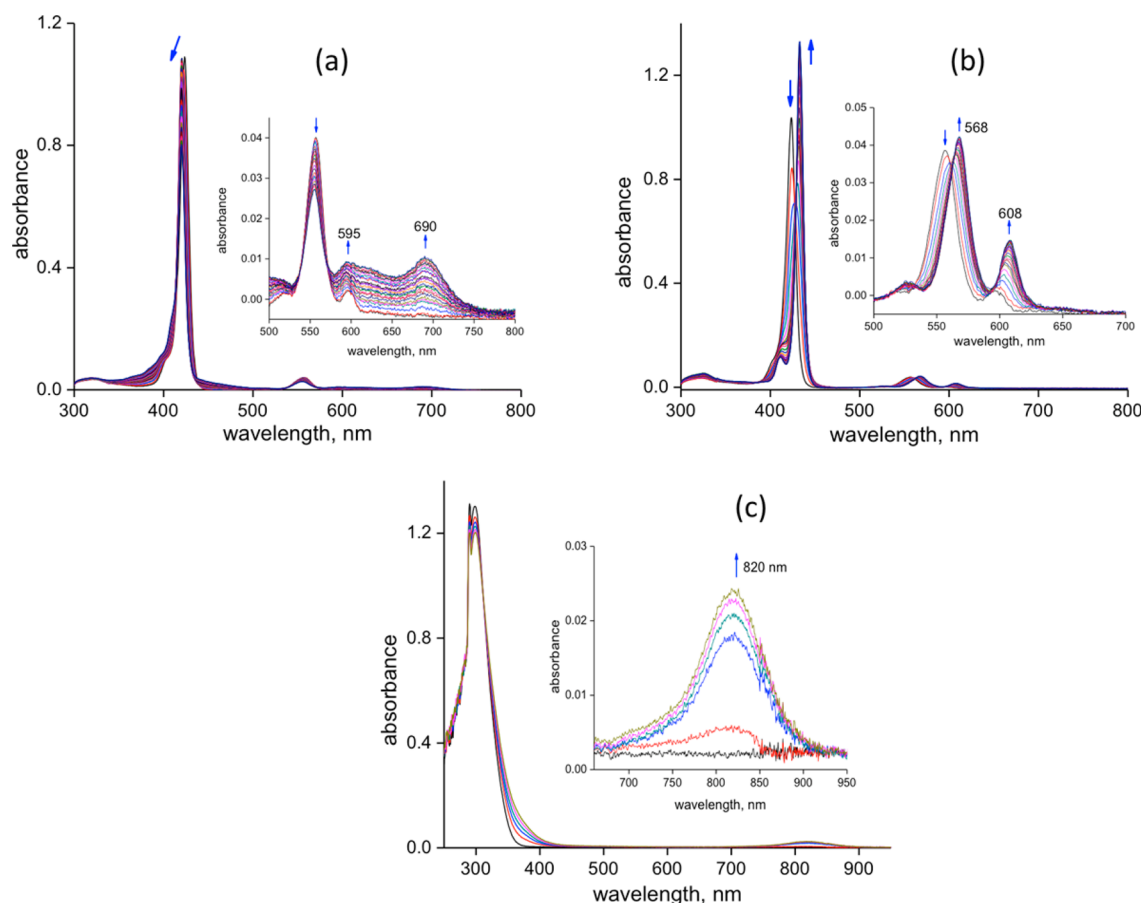


Figure 6. Spectral changes observed during the (a) first oxidation of AlPor-Ph, (b) first reduction of AlPor-Ph, and (c) first oxidation of BAA-Py in *o*-DCB with 0.2 M TBA·ClO₄.

peak of BAA-Py was located at 820 nm. Isosbestic points at 288 and 312 nm were also observed. The reversible formation of cationic and anionic species of the sensitizer and hole transporting agent indicates their robust nature and as good sensitizers for the intended studies.

Transient Absorption Spectroscopy. First, femtosecond transient spectra of AlPor in both the absence and presence of BAA-Py were recorded to explore the possibility of electron transfer from BAA-Py to photoexcited ¹AlPor*. Figures 7a and S8a in the Supporting Information, respectively, show the transient spectra at the indicated delay times for AlPor-Ph and AlPor-Ph-HMAH in Ar-saturated toluene in the absence of BAA-Py. In both cases, the instantaneous formation of ¹AlPor* leads to positive peaks at 452, 580, 613, and 1238 nm accompanied by negative peaks at 556, 595, and 650 nm. The peak at 556 nm corresponds to the ground state bleaching, while the latter two peaks are due to stimulated emission. The near-IR peak at 1238 nm is due to singlet-singlet absorption of ¹AlPor*, similar to that reported earlier to other AlPor systems.^{37–39} The decay of the positive peaks and recovery of the negative stimulated emission peak is accompanied by new peaks at 458 and 840 nm, which are characteristic of ³AlPor* according to both the literature^{37–39} and our DFT calculations which place the T₁ → S₀ at 864 nm. Coordinating the electron donor, BAA-Py, to AlPor-Ph and AlPor-Ph-HMAH revealed transient spectra very similar to that of the pristine AlPor (see Figures 7b and S8b in the Supporting Information). That is, instantaneous formation of ¹AlPor*, followed by

intersystem crossing to populate the ³AlPor*, is observed. Figure 7c and d shows the decay profile of the 1238 nm peak for the AlPor-Ph and AlPor-Ph-HMAH, respectively, without (red trace) and with (blue trace) coordinated BAA-Py. Addition of BAA-Py causes only a very slight increase in the rate of decay of the ¹AlPor* state, which is consistent with the small decrease in the steady-state fluorescence, suggesting that any photochemical processes associated with BAA are slow compared to intersystem crossing. These results were also supported by fluorescence lifetime of ¹AlPor* recorded in the absence and presence of BAA-Py. The fluorescence lifetimes (all of them exhibited monoexponential decay) of AlPor-Ph and AlPor-Ph-HMAH in *o*-DCB were found to be 3.35 and 3.48 ns, respectively, which were reduced to 3.29 and 3.40 ns suggesting only a moderate amount of quenching.

Figure 8a illustrates the femtosecond transient spectra of AlPor-OH immobilized on TiO₂ surface (see Experimental Section for details) at different delay times. At the excitation wavelength of 400 nm only AlPor of AlPor-TiO₂ was being excited. Compared to the isolated AlPor in solution, much larger absorbance changes and a faster recovery of the ground state are observed when AlPor is bound to as TiO₂. Importantly, no peaks corresponding to stimulated emission at 595 and 650 nm were observed. This implies that ¹AlPor* is involved in ultrafast photoinduced events involving TiO₂ instead of undergoing radiative decay. The broad absorbance increase at wavelengths longer than the Q-band bleach at 556 nm with a maximum around 690 nm is characteristic of the absorption of AlPor^{•+} (see the spectra recorded at 800 fs and 1

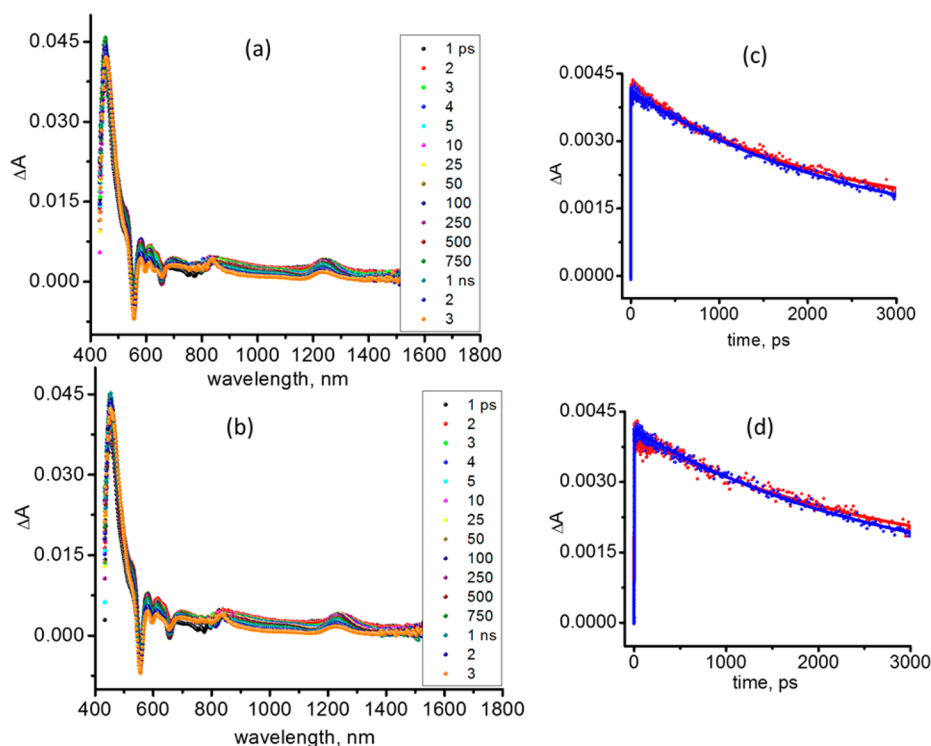


Figure 7. Femtosecond transient spectra of AlPor-Ph (a) in the absence and (b) in the presence of BAA-Py at the indicated delay times in Ar-saturated toluene. Panels c and d show decay profile of the 1238 nm peak in the absence (red) and presence (blue) of BAA-Py bound to AlPor-Ph and AlPor-Ph-HMAH, respectively.

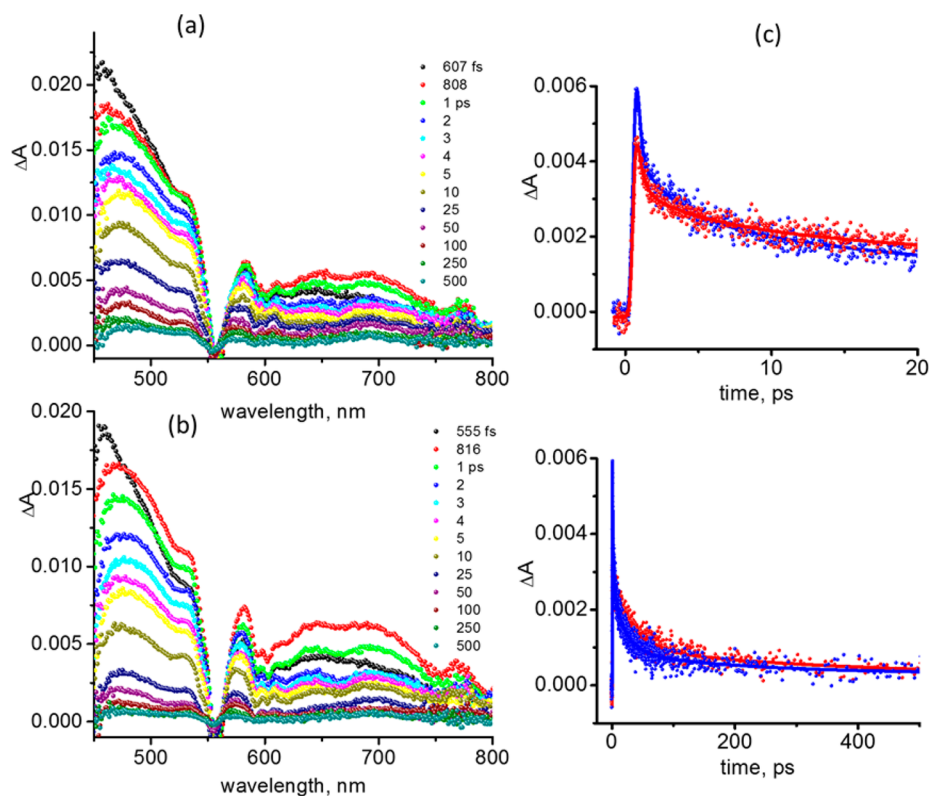


Figure 8. Femtosecond transient absorption spectra of (a) AlPor-TiO₂ and (b) BAA-Py-AlPor-TiO₂ at the indicated delay times and (c) the decay profiles of the 690 nm peak corresponding to AlPor^{•+} rise (top panel) and decay (bottom panel) in the case of AlPor-TiO₂ (red) and BAA-Py-AlPor-TiO₂ (blue), respectively.

ps delay times in Figure 8a and the spectrum of AlPor^{•+} in Figure 6a) and provides evidence of fast charge injection from

¹AlPor* to TiO₂. The absorbances of the injected electrons in the conduction band of TiO₂ are known to appear in the mid-

IR⁵⁶ and THz regions^{57,58} beyond the monitoring window of our spectrometer. The growth and decay of the 690 nm band due to AlPor^{•+} was monitored to evaluate the time constant and rates of formation (k_f) and decay (k_D), as shown in Figure 8c (red line). Immediately after excitation, the absorbance change at 690 nm is due to ¹AlPor*, which decays within about 1 ps as AlPor^{•+} is formed. AlPor^{•+} then decays in about 70 ps. The fit to the red time trace in Figure 8c yields time constants of 1.7 and 73.8 ps, respectively, for charge injection and recombination. This resulted in k_f and k_D values of $6.0 \times 10^{11} \text{ s}^{-1}$ and $13.5 \times 10^9 \text{ s}^{-1}$, respectively (Table 2).

Table 2. Evaluation of the Time Constants and Rates of Formation, k_f , and Decay, k_D , of AlPor^{•+} on the Modified TiO₂ Surfaces (Estimated Error $\pm 5\%$)

substrate	time constants		rate constants	
	τ_f , ps	τ_D , ps	k_f , s ⁻¹	k_D , s ⁻¹
AlPor–TiO ₂	1.7	73.8	6.0×10^{11}	13.5×10^9
BAA–Py–AlPor–TiO ₂	0.7	55.8	14.5×10^{11}	17.9×10^9
AlPor–Ph–TiO ₂	2.1	100.0	4.9×10^{11}	9.9×10^9
BAA–Py–AlPor–Ph–TiO ₂	1.8	81.0	5.5×10^{11}	12.3×10^9

The binding of BAA–Py to AlPor–TiO₂ results in the formation of BAA–Py–AlPor–TiO₂ wherein the BAA–Py can act as a secondary electron donor. The successful binding of BAA–Py to AlPor is easily monitored by the color change of the AlPor–TiO₂ electrodes before and after soaking in BAA–Py (see Figure 5c and d). As discussed above, electron transfer from BAA to ¹AlPor* in BAA–Py–AlPor is slow compared to intersystem crossing and therefore 3–4 orders of magnitude slower than the electron injection in AlPor–TiO₂. Based on

this, the photoexcitation of BAA–Py–AlPor–TiO₂ should initially undergo fast charge injection from ¹AlPor* into the conduction band of TiO₂. However, it is unclear whether electron transfer from BAA–Py to AlPor^{•+} can outcompete back electron transfer from TiO₂. If it does, then the overall lifetime of AlPor^{•+} will become shorter. Figure 8b shows the transient absorption spectra at the indicated delay times of BAA–Py–AlPor–TiO₂. The spectral features are close to those observed in AlPor–TiO₂ in Figure 8a; however, the spectra are 3–4 nm red-shifted due to the presence of the axially bound ligand. By monitoring the growth and decay of the 690 nm peak due to AlPor^{•+}, the time constant and rates of formation and decay, k_f and k_D , were evaluated; see Figure 8c (blue line). Faster charge injection compared to that obtained in the absence of BAA–Py coordination was witnessed; see Table 2. The time constants were found to be 0.7 and 55.8 ps, respectively, for the formation and decay of AlPor^{•+}. This resulted in k_f and k_D values of $14.5 \times 10^{11} \text{ s}^{-1}$ and $17.9 \times 10^9 \text{ s}^{-1}$, respectively.

Next, AlPor–Ph–HMAH was studied as bound on TiO₂ with femtosecond transient spectral measurements, in the absence and presence of BAA–Py. Due to the Ph–HMAH binding motif, the distance between the TiO₂ surface and AlPor is expected to be about $\sim 8 \text{ \AA}$ more than for AlPor–TiO₂. Figure 9a shows transient spectra of AlPor–Ph–TiO₂ modified surface at the indicated delay times. Again, the spectra show features associated with AlPor^{•+} suggesting that electron injection into the semiconductor occurs. The time constants obtained by fitting the time profile at 690 nm (Figure 9c red trace) were found to be 2.1 and 100 ps, respectively, for the formation and decay of AlPor^{•+}. This resulted in k_f and k_D values of $4.9 \times 10^{11} \text{ s}^{-1}$ and $9.9 \times 10^9 \text{ s}^{-1}$, respectively. Due to the increased distance between the sensitizer and TiO₂, the k_f

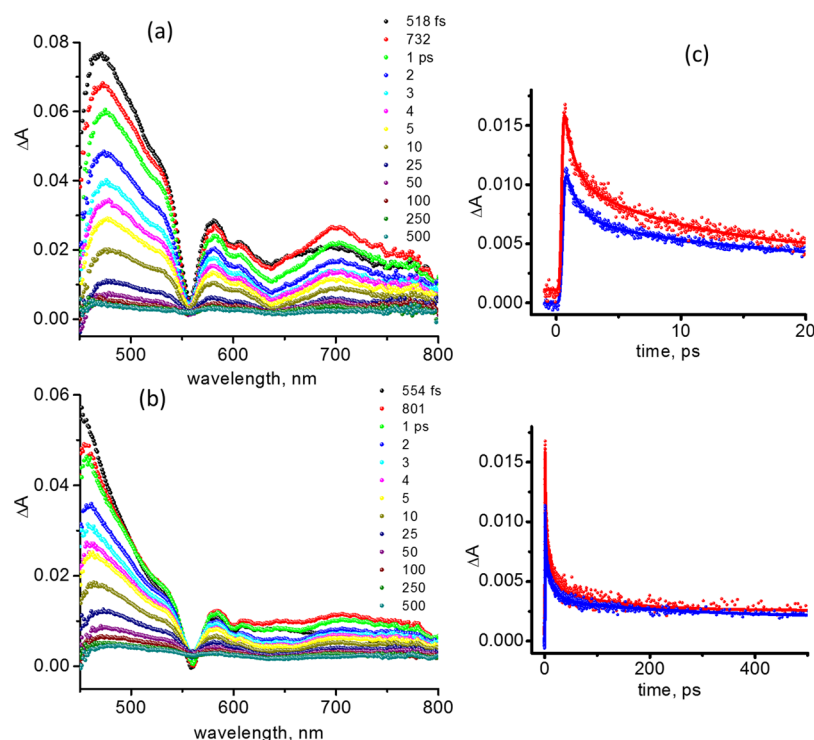


Figure 9. Femtosecond transient absorption spectra of (a) AlPor–Ph–TiO₂ and (b) BAA–Py–AlPor–Ph–TiO₂ at the indicated delay times. Panel c shows the decay profiles of the 690 nm peak corresponding to AlPor^{•+} rise (top panel) and decay (bottom panel) in the case of AlPor–Ph–TiO₂ (red) and BAA–Py–AlPor–Ph–TiO₂ (blue), respectively.

and k_D values are lower in AlPor–Ph–TiO₂ than in AlPor–TiO₂. The transient spectral features upon coordinating BAA–Py to AlPor–Ph–TiO₂ (Figure 9b) again suggest charge injection from the ¹AlPor*, and as seen with AlPor–TiO₂, the formation and decay of AlPor^{•+} are faster when BAA–Py is coordinated (see Table 2 and Figure 9c).

It is clear from these data that coordinating BAA–Py accelerates both charge injection and decay processes in the case of both the AlPor–TiO₂ and AlPor–Ph–TiO₂ systems. Having a spacer between AlPor and TiO₂ slows down the rates to some extent due to increased distance. However, the magnitude of the charge injection process clearly indicates ultrafast process originating from AlPor making them a viable alternative to commonly used ZnPor based sensitizers for dye sensitized solar cell applications. We note also that, in both Figures 8c and 9c, there is a short-lived component that could be ascribed to ¹AlPor* that is overlapping with the AlPor^{•+} signal. Additionally, the signal does not decay to zero even at 500 ps suggesting the possibility of a minor, slow charge recombination component.

Interfacial Electron Transfer Calculations. The injection of photoexcited electrons into anatase TiO₂ was studied computationally on semioptimized porphyrin–TiO₂ systems. This methodology has been shown to accurately capture the injection rate trend between different species.⁵⁹ The survival probability of the wave packet on the adsorbate is presented in Figure 10, where fitting to an exponential decay function results

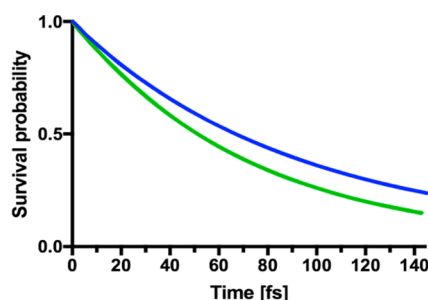


Figure 10. Survival probability of a wave packet initialized on either the porphyrin LUMO (blue) or LUMO+1 (green) in the AlPor–Ti₁₂₈O₂₅₆ system.

in an injection rate k_f of $11.2 \times 10^{12} \text{ s}^{-1}$ for LUMO and $13.8 \times 10^{12} \text{ s}^{-1}$ for LUMO+1. This is considerably faster than observed experimentally, which is typical for this methodology and is attributed to the neglect of effects such as orbital relaxation, thermal structural fluctuations, and electron–phonon coupling. The AlPor–Ph–TiO₂ system showed minimal injection on the time scale of the simulation, but fitting and extrapolation nevertheless yielded an estimated injection lifetime of $1.8 \times 10^9 \text{ s}^{-1}$ for LUMO and $8.42 \times 10^7 \text{ s}^{-1}$ for LUMO+1. This slow injection is attributed to the minimal coupling between the perpendicular π -systems of the porphyrin and longer Ph–HMA bridge. This small coupling is consistent with experimental observations: the linker infers minimal influence on the optical and electrochemical properties of the porphyrin, as discussed earlier in this article. Thermal fluctuations confer an increased average coupling under experimental conditions, but computational consideration of such effects is beyond the scope of the current study.

CONCLUSIONS

The results presented here show that the unique properties of AlPor can be exploited for construction of “self-assembled” photoanodes on TiO₂ surface. In these photoanodes, AlPor is covalently linked to the TiO₂ surface, while the BAA–Py is coordinated to the Al center through Lewis acid–base interactions. This strategy provides vertical arrangement of chromophore and secondary electron donor on the metal oxide surface. With time-resolved spectroscopy and electron-dynamics calculations we show that, upon photoexcitation with visible light, ultrafast electron injection takes place from AlPor into the conduction band of TiO₂, and this is followed by photo-oxidation of the secondary electron donor BAA–Py. The later process made possible due to formation of AlPor^{•+}, which holds enough anodic potential to oxidize the coordinated secondary electron donor (BAA–Py). Ultimately, our self-assembly strategy provides a way to attach a water oxidation catalyst, by replacing the secondary electron donor, to a photosensitizer on the metal oxide surface. At the same time, our analysis shows that additional work is needed to optimize the electron-transfer process as required for water oxidation. Currently, we are using various secondary electron donors, with lower oxidation potentials than BAA–Py, to study the sequential electron transfer in self-assembled photoanodes.

ASSOCIATED CONTENT

Supporting Information

The Supporting Information is available free of charge on the ACS Publications website at DOI: 10.1021/acs.jpcc.7b04197.

Synthesis, structural characterization, NMR spectra, calculated absorption transitions, isodensity plots of the frontier orbitals, absorption and fluorescence titrations, and transient absorption spectra (PDF)

AUTHOR INFORMATION

Corresponding Authors

*E-mail: victor.batista@yale.edu.

*E-mail: Francis.DSouza@UNT.edu.

*E-mail: avde@brocku.ca.

*E-mail: ppoddutoori@upei.ca.

ORCID

Victor S. Batista: 0000-0002-3262-1237

Francis D'Souza: 0000-0003-3815-8949

Prashanth K. Poddutoori: 0000-0001-6007-8801

Present Address

S.H.: Fysikum, Stockholm University, 10691 Stockholm, Sweden.

Notes

The authors declare no competing financial interest.

ACKNOWLEDGMENTS

This work was supported by the Natural Science and Engineering Research Council of Canada (AvdE), the Department of Chemistry, University of Prince Edward Island, Canada (PPK), and the US-National Science Foundation (grant no. 1401188 to F.D.). S.H., K.A.J., and V.S.B. thank the US Department of Energy, Office of Science, under grant no. DE-FG02-07ER15909 for funding, the TomKat Charitable Trust for a generous donation, and Yale HPC for computer resources used.

REFERENCES

- (1) Gust, D.; Moore, T. A.; Moore, A. L. Solar Fuels Via Artificial Photosynthesis. *Acc. Chem. Res.* **2009**, *42*, 1890–1898.
- (2) Hammarstrom, L.; Hammes-Schiffer, S. Artificial Photosynthesis and Solar Fuels. *Acc. Chem. Res.* **2009**, *42*, 1859–1860.
- (3) Armaroli, N.; Balzani, V. The Future of Energy Supply: Challenges and Opportunities. *Angew. Chem., Int. Ed.* **2007**, *46*, 52–66.
- (4) Crabtree, G. W.; Lewis, N. S. Solar Energy Conversion. *Phys. Today* **2007**, *60*, 37–42.
- (5) Lewis, N. S.; Nocera, D. G. Powering the Planet: Chemical Challenges in Solar Energy Utilization. *Proc. Natl. Acad. Sci. U. S. A.* **2006**, *103*, 15729–15735.
- (6) Moore, G. F.; Brudvig, G. W. Energy Conversion in Photosynthesis: A Paradigm for Solar Fuel Production. *Annu. Rev. Condens. Matter Phys.* **2011**, *2*, 303–327.
- (7) Roy, S. C.; Varghese, O. K.; Paulose, M.; Grimes, C. A. Toward Solar Fuels: Photocatalytic Conversion of Carbon Dioxide to Hydrocarbons. *ACS Nano* **2010**, *4*, 1259–1278.
- (8) Sun, L. C.; Hammarstrom, L.; Akermark, B.; Styring, S. Towards Artificial Photosynthesis: Ruthenium-Manganese Chemistry for Energy Production. *Chem. Soc. Rev.* **2001**, *30*, 36–49.
- (9) Alibabaei, L.; Brennaman, M. K.; Norris, M. R.; Kalanyan, B.; Song, W. J.; Losego, M. D.; Concepcion, J. J.; Binstead, R. A.; Parsons, G. N.; Meyer, T. J. Solar Water Splitting in a Molecular Photoelectrochemical Cell. *Proc. Natl. Acad. Sci. U. S. A.* **2013**, *110*, 20008–20013.
- (10) Gao, Y.; Ding, X.; Liu, J. H.; Wang, L.; Lu, Z. K.; Li, L.; Sun, L. C. Visible Light Driven Water Splitting in a Molecular Device with Unprecedentedly High Photocurrent Density. *J. Am. Chem. Soc.* **2013**, *135*, 4219–4222.
- (11) Young, K. J.; Martini, L. A.; Milot, R. L.; Snoeberger, R. C.; Batista, V. S.; Schmittenmaer, C. A.; Crabtree, R. H.; Brudvig, G. W. Light-Driven Water Oxidation for Solar Fuels. *Coord. Chem. Rev.* **2012**, *256*, 2503–2520.
- (12) Youngblood, W. J.; Lee, S. H. A.; Kobayashi, Y.; Hernandez-Pagan, E. A.; Hoertz, P. G.; Moore, T. A.; Moore, A. L.; Gust, D.; Mallouk, T. E. Photoassisted Overall Water Splitting in a Visible Light-Absorbing Dye-Sensitized Photoelectrochemical Cell. *J. Am. Chem. Soc.* **2009**, *131*, 926–927.
- (13) Meyer, T. J.; Alibabaei, L.; Brennaman, M. K.; Norris, M. R.; Kalanyan, B.; Song, W. J.; Losego, M. D.; Concepcion, J. J.; Binstead, R. A.; Parsons, G. N. Solar Water Splitting in a Molecular Photoelectrochemical Cell. *Abstr. Pap. Am. Chem. Soc.* **2014**, 247.
- (14) Bignozzi, C. A.; Argazzi, R.; Boaretto, R.; Busatto, E.; Carli, S.; Ronconi, F.; Caramori, S. The Role of Transition Metal Complexes in Dye Sensitized Solar Devices. *Coord. Chem. Rev.* **2013**, *257*, 1472–1492.
- (15) Gratzel, M. Recent Advances in Sensitized Mesoscopic Solar Cells. *Acc. Chem. Res.* **2009**, *42*, 1788–1798.
- (16) Kim, B. G.; Chung, K.; Kim, J. Molecular Design Principle of All-Organic Dyes for Dye-Sensitized Solar Cells. *Chem. - Eur. J.* **2013**, *19*, 5220–5230.
- (17) Zhao, Y. X.; et al. Improving the Efficiency of Water Splitting in Dye-Sensitized Solar Cells by Using a Biomimetic Electron Transfer Mediator. *Proc. Natl. Acad. Sci. U. S. A.* **2012**, *109*, 15612–15616.
- (18) Obraztsov, I.; Kutner, W.; D'Souza, F. Evolution of Molecular Design of Porphyrin Chromophores for Photovoltaic Materials of Superior Light-to-Electricity Conversion Efficiency. *Solar RRL* **2017**, *1*, 1600002.
- (19) Martini, L. A.; Moore, G. F.; Milot, R. L.; Cai, L. Z.; Sheehan, S. W.; Schmittenmaer, C. A.; Brudvig, G. W.; Crabtree, R. H. Modular Assembly of High-Potential Zinc Porphyrin Photosensitizers Attached to TiO₂ with a Series of Anchoring Groups. *J. Phys. Chem. C* **2013**, *117*, 14526–14533.
- (20) Milot, R. L.; Moore, G. F.; Crabtree, R. H.; Brudvig, G. W.; Schmittenmaer, C. A. Electron Injection Dynamics from Photoexcited Porphyrin Dyes into SnO₂ and TiO₂ Nanoparticles. *J. Phys. Chem. C* **2013**, *117*, 21662–21670.
- (21) Moore, G. F.; Konezny, S. J.; Song, H. E.; Milot, R. L.; Blakemore, J. D.; Lee, M. L.; Batista, V. S.; Schmittenmaer, C. A.; Crabtree, R. H.; Brudvig, G. W. Bioinspired High-Potential Porphyrin Photoanodes. *J. Phys. Chem. C* **2012**, *116*, 4892–4902.
- (22) Higashino, T.; Imahori, H. Porphyrins as Excellent Dyes for Dye-Sensitized Solar Cells: Recent Developments and Insights. *Dalton Trans.* **2015**, *44*, 448–463.
- (23) Jiang, J.; Swierk, J. R.; Materna, K. L.; Hedström, S.; Lee, S. H.; Crabtree, R. H.; Schmittenmaer, C. A.; Batista, V. S.; Brudvig, G. W. High-Potential Porphyrins Supported on SnO₂ and TiO₂ Surfaces for Photoelectrochemical Applications. *J. Phys. Chem. C* **2016**, *120*, 28971–28982.
- (24) Moore, G. F.; Blakemore, J. D.; Milot, R. L.; Hull, J. F.; Song, H. E.; Cai, L.; Schmittenmaer, C. A.; Crabtree, R. H.; Brudvig, G. W. A Visible Light Water-Splitting Cell with a Photoanode Formed by Codeposition of a High-Potential Porphyrin and an Iridium Water-Oxidation Catalyst. *Energy Environ. Sci.* **2011**, *4*, 2389–2392.
- (25) Poddutoori, P. K.; Thomsen, J. M.; Milot, R. L.; Sheehan, S. W.; Negre, C. F. A.; Garapati, V. K. R.; Schmittenmaer, C. A.; Batista, V. S.; Brudvig, G. W.; van der Est, A. Interfacial Electron Transfer in Photoanodes Based on Phosphorus(V) Porphyrin Sensitizers Co-Deposited on SnO₂ with the Ir(III)Cp* Water Oxidation Precatalyst. *J. Mater. Chem. A* **2015**, *3*, 3868–3879.
- (26) Nayak, A.; Knauf, R. R.; Hanson, K.; Alibabaei, L.; Concepcion, J. J.; Ashford, D. L.; Dempsey, J. L.; Meyer, T. J. Synthesis and Photophysical Characterization of Porphyrin and Porphyrin-Ru(II) Polypyridyl Chromophore-Catalyst Assemblies on Mesoporous Metal Oxides. *Chem. Sci.* **2014**, *5*, 3115–3119.
- (27) Yamamoto, M.; Wang, L.; Li, F. S.; Fukushima, T.; Tanaka, K.; Sun, L. C.; Imahori, H. Visible Light-Driven Water Oxidation Using a Covalently-Linked Molecular Catalyst-Sensitizer Dyad Assembled on a TiO₂ Electrode. *Chem. Sci.* **2016**, *7*, 1430–1439.
- (28) Negre, C. F. A.; Milot, R. L.; Martini, L. A.; Ding, W.; Crabtree, R. H.; Schmittenmaer, C. A.; Batista, V. S. Efficiency of Interfacial Electron Transfer from Zn-Porphyrin Dyes into TiO₂ Correlated to the Linker Single Molecule Conductance. *J. Phys. Chem. C* **2013**, *117*, 24462–24470.
- (29) Rochford, J.; Chu, D.; Hagfeldt, A.; Galoppini, E. Tetrachelate Porphyrin Chromophores for Metal Oxide Semiconductor Sensitization: Effect of the Spacer Length and Anchoring Group Position. *J. Am. Chem. Soc.* **2007**, *129*, 4655–4665.
- (30) Choi, H.; Cho, N.; Paek, S.; Ko, J. Direct Evidence of Forster Resonance Energy Transfer for the Enhanced Photocurrent Generation in Dye-Sensitized Solar Cell. *J. Phys. Chem. C* **2014**, *118*, 16319–16327.
- (31) Pelleja, L.; Kumar, C. V.; Clifford, J. N.; Palomares, E. D-Pi-Porphyrin Employing an Indoline Donor Group for High Efficiency Dye-Sensitized Solar Cells. *J. Phys. Chem. C* **2014**, *118*, 16504–16509.
- (32) Gobeze, H. B.; Das, S. K.; D'Souza, F. Femtosecond Transient Absorption Study of Supramolecularly Assembled Metal Tetrapyrrole-TiO₂ Thin Films. *J. Phys. Chem. C* **2014**, *118*, 16660–16671.
- (33) Millesi, S.; Lo Nigro, R.; Pedroni, M.; Speghini, A.; Gulino, A. Photoexcited Porphyrins Functionalizing TiO₂ and SnO₂ Nanocrystals. *J. Phys. Chem. C* **2015**, *119*, 23743–23751.
- (34) Kadish, K. M.; Smith, K. M.; Guillard, R. *Handbook of Porphyrin Science*; World Scientific: Singapore, 2010.
- (35) Poddutoori, P. K.; Poddutoori, P.; Maiya, B. G.; Prasad, T. K.; Kandrashkin, Y. E.; Vasil'ev, S.; Bruce, D.; van der Est, A. Redox Control of Photoinduced Electron Transfer in Axial Terpyridoxy Porphyrin Complexes. *Inorg. Chem.* **2008**, *47*, 7512–7522.
- (36) Kumar, P. P.; Maiya, B. G. Aluminium(III) Porphyrin Based Dimers and Trimers: Synthesis, Spectroscopy and Photochemistry. *New J. Chem.* **2003**, *27*, 619–625.
- (37) Poddutoori, P. K.; Bregles, L. P.; Lim, G. N.; Boland, P.; Kerr, R. G.; D'Souza, F. Modulation of Energy Transfer into Sequential Electron Transfer Upon Axial Coordination of Tetrathiafulvalene in an Aluminium(III) Porphyrin-Free-Base Porphyrin Dyad. *Inorg. Chem.* **2015**, *54*, 8482–8494.

- (38) Poddutoori, P. K.; Lim, G. N.; Sandanayaka, A. S. D.; Karr, P. A.; Ito, O.; D'Souza, F.; Pilkington, M.; van der Est, A. Axially Assembled Photosynthetic Reaction Center Mimics Composed of Tetrathiafulvalene, Aluminum(III) Porphyrin and Fullerene Entities. *Nanoscale* **2015**, *7*, 12151–12165.
- (39) Poddutoori, P. K.; Lim, G. N.; Vassiliev, S.; D'Souza, F. Ultrafast Charge Separation and Charge Stabilization in Axially Linked Letrathiafulvalene-Aluminum(III) Porphyrin-Gold(III) Porphyrin' Reaction Center Mimics. *Phys. Chem. Chem. Phys.* **2015**, *17*, 26346–26358.
- (40) Poddutoori, P. K.; Sandanayaka, A. S. D.; Hasobe, T.; Ito, O.; van der Est, A. Photoinduced Charge Separation in a Ferrocene-Aluminum(III) Porphyrin-Fullerene Supramolecular Triad. *J. Phys. Chem. B* **2010**, *114*, 14348–14357.
- (41) Poddutoori, P. K.; Sandanayaka, A. S. D.; Zarrabi, N.; Hasobe, T.; Ito, O.; van der Est, A. Sequential Charge Separation in Two Axially Linked Phenothiazine-Aluminum(III) Porphyrin-Fullerene Triads. *J. Phys. Chem. A* **2011**, *115*, 709–717.
- (42) Poddutoori, P. K.; Zarrabi, N.; Moiseev, A. G.; Gumbau-Brisa, R.; Vassiliev, S.; van der Est, A. Long-Lived Charge Separation in Novel Axial Donorporphyrinacceptor Triads Based on Tetrathiafulvalene, Aluminum(III) Porphyrin and Naphthalenediimide. *Chem. - Eur. J.* **2013**, *19*, 3148–3161.
- (43) Brewster, T. P.; Konezny, S. J.; Sheehan, S. W.; Martini, L. A.; Schmuttenmaer, C. A.; Batista, V. S.; Crabtree, R. H. Hydroxamate Anchors for Improved Photoconversion in Dye-Sensitized Solar Cells. *Inorg. Chem.* **2013**, *52*, 6752–6764.
- (44) McNamara, W. R.; Milot, R. L.; Song, H. E.; Snoeberger, R. C.; Batista, V. S.; Schmuttenmaer, C. A.; Brudvig, G. W.; Crabtree, R. H. Water-Stable, Hydroxamate Anchors for Functionalization of TiO₂ Surfaces with Ultrafast Interfacial Electron Transfer. *Energy Environ. Sci.* **2010**, *3*, 917–923.
- (45) Lindsey, J. S.; Schreiman, I. C.; Hsu, H. C.; Kearney, P. C.; Marguerettaz, A. M. Rothmund and Adler-Longo Reactions Revisited - Synthesis of Tetraphenylporphyrins under Equilibrium Conditions. *J. Org. Chem.* **1987**, *52*, 827–836.
- (46) Thordarson, P. Determining Association Constants from Titration Experiments in Supramolecular Chemistry. *Chem. Soc. Rev.* **2011**, *40*, 1305–1323.
- (47) Frisch, M. J., et al. *Gaussian 09*; Gaussian Inc.: Wallingford, CT, 2009.
- (48) Su, P.; Li, H. Continuous and Smooth Potential Energy Surface for Conductorlike Screening Solvation Model Using Fixed Points with Variable Areas. *J. Chem. Phys.* **2009**, *130*, 074109.
- (49) Becke, A. D. Density-Functional Thermochemistry 0.3. The Role of Exact Exchange. *J. Chem. Phys.* **1993**, *98*, 5648–5652.
- (50) McNaught, A. D.; Wilkinson, A. *Iupac. Compendium of Chemical Terminology*, 2nd ed. (the "Gold Book"); Blackwell Scientific Publications: Oxford, 1997.
- (51) Kumar, P. P.; Premaladha, G.; Maiya, B. G. Porphyrin-Anthraquinone Dyads: Synthesis, Spectroscopy and Photochemistry. *J. Chem. Sci.* **2005**, *117*, 193–201.
- (52) Yanai, T.; Tew, D. P.; Handy, N. C. A New Hybrid Exchange-Correlation Functional Using the Coulomb-Attenuating Method (Cam-B3lyp). *Chem. Phys. Lett.* **2004**, *393*, 51–57.
- (53) Rego, L. G. C.; Batista, V. S. Quantum Dynamics Simulations of Interfacial Electron Transfer in Sensitized TiO₂ Semiconductors. *J. Am. Chem. Soc.* **2003**, *125*, 7989–7997.
- (54) Landrum, G. A.; Glassey, W. V. *bind 3.0* in YAEHMOP, <https://sourceforge.net/projects/yaehmop>.
- (55) Rothenberger, G.; Fitzmaurice, D.; Graetzel, M. Spectroscopy of Conduction Band Electrons in Transparent Metal Oxide Semiconductor Films: Optical Determination of the Flatband Potential of Colloidal Titanium Dioxide Films. *J. Phys. Chem.* **1992**, *96*, 5983–5986.
- (56) Ghosh, H. N.; Asbury, J. B.; Lian, T. Direct Observation of Ultrafast Electron Injection from Coumarin 343 to TiO₂ Nanoparticles by Femtosecond Infrared Spectroscopy. *J. Phys. Chem. B* **1998**, *102*, 6482–6486.
- (57) Hendry, E.; Wang, F.; Shan, J.; Heinz, T. F.; Bonn, M. Electron Transport in Tio 2 Probed by Thz Time-Domain Spectroscopy. *Phys. Rev. B: Condens. Matter Mater. Phys.* **2004**, *69*, 081101.
- (58) Richter, C.; Schmuttenmaer, C. A. Exciton-Like Trap States Limit Electron Mobility in TiO₂ Nanotubes. *Nat. Nanotechnol.* **2010**, *5*, 769–772.
- (59) Jiang, J. B.; Swierk, J. R.; Hedstrom, S.; Matula, A. J.; Crabtree, R. H.; Batista, V. S.; Schmuttenmaer, C. A.; Brudvig, G. W. Molecular Design of Light-Harvesting Photosensitizers: Effect of Varied Linker Conjugation on Interfacial Electron Transfer. *Phys. Chem. Chem. Phys.* **2016**, *18*, 18678–18682.